Eggbauer, A.; Lukas, M.; Ressel, G.; Prevedel, P.; Mendez-Martin, F.; Keckes, J.; Stark, A.; Ebner, R.:

In situ analysis of the effect of high heating rates and initial microstructure on the formation and homogeneity of austenite.

In: Journal of Materials Science. Vol. 54 (2019) 9197 - 9212.

First published online by Springer: 22.03.2019

https://dx.doi.org/10.1007/s10853-019-03527-3

In-situ analysis of the effect of high heating rates and initial microstructure on the formation and homogeneity of austenite

Annika Eggbauer[1]*, Marina Lukas[1], Gerald Ressel[1], Petri Prevedel[1], Francisca Martin-Mendez[2], Jozef Keckes[3], Andreas Stark[4], Reinhold Ebner[1]

[1] Materials Center Leoben Forschung GmbH, Roseggerstrasse 12, 8700 Leoben, Austria

[2]Department of Physical Metallurgy and Materials Testing, Montanuniversität Leoben, Franz Josef Strasse 18, 8700 Leoben, Austria

[3] Department of Materials Physics, Montanuniversität Leoben, and Erich Schmid Institute of Materials Science, 8700 Leoben, Austria

[4]Helmholtz Zentrum Geesthacht, Institute of Materials Research, Max Planck Straße 1, 21502 Geesthacht, Germany

* Corresponding author; e-mail address: Annikaeggbauer@gmail.com

1. **Abstract**

Decreasing processing time of a quench and temper heat treatment is of high interest for industry due to the possibility of cost reduction. One option to reduce processing time is to shorten the austenitizing cycle by applying high heating rates and minimum holding times. However, due to the high heating rates, the analysis of their influences on the formation kinetics of austenite and its crystallographic parameters is challenging.

Thus, this work concentrates on the *in-situ* analysis of the austenitization process by means of high energy X-ray diffraction to study a range of heating rates applied to ferritic-pearlitic and soft annealed initial microstructures. The transformation kinetics from ferrite/pearlite and soft annealed state to austenite, the cementite dissolution behavior and the homogeneity of the freshly
formed austenite were analyzed.

The results indicate three distinct steps of austenite formation independent of initial microstructure and heating rate: (i) nucleation of carbon rich austenite at cementite- ferrite interfaces, (ii) growth of austenite phase fraction accompanied by a reduction of the carbon content, until reaching the mean carbon content of the steel, followed by growth of the austenite grain size, (iii). Regarding austenite homogeneity, the combination of austenitization temperature and initial microstructure are the main influencing factors.

2. **Introduction**

Accelerating heat treatment processes without reduction of mechanical properties or microstructural features compared to slower processes is of high interest for the heat treating industry. One possibility to save process time in heat treatment of quenched and tempered (QT) steels is to shorten the austenitizing time prior to quenching, for example by induction heating. However, there are some indications that fast austenitizing leads to lower yield strength in the martensitic state compared to conventional austenitizing [1]. It is suggested that the lower yield strength results from reduced austenite homogeneity and higher distortions within the freshly formed martensite than in conventional heat treatment that exhibits slower heating rates and extended holding times at austenitization temperature [1, 2].

It is reported in literature that transformation temperatures of bcc to fcc increase with increasing heating rate and that the initial microstructure has an important influence on the austenite formation kinetics [3, 4, 5, 6, 7, 8, 9]. The austenite formation temperature increases in the following order: martensite exhibits the lowest austenite start temperature, followed by bainite, then by ferrite-pearlite, and the soft annealed state exhibits the highest austenite start temperature [10]. In [5, 11] a two-stage austenite formation was proven for a ferritic- pearlitic initial microstructure: (i) the austenite nucleates at the interfaces of pearlite grain boundaries or at the interfaces between ferrite and cementite lamella and then rapidly grows into the pearlite, and (ii) the remaining ferritic areas are transformed into austenite. Esin et al [4] investigated the steps of austenite formation for three different initial microstructures (ferrite-pearlite, bainite and tempered martensite) of a 0.36C-1.25Mn- 0.70Cr- 0.12V-0.07Mo-steel at different heating rates. They concluded that the transformation temperatures are more affected by the initial microstructure than by the heating rate. With increasing heating rate the transformation temperatures increase more distinctly for a ferritic-

pearlitic initial microstructure than for a bainitic initial microstructure. Additionally, the ferritic-pearlitic initial microstructure showed overlapping of the transformation stages ((i) growth of austenite into pearlite and (ii) into the ferritic areas) with increasing heating rate. Such an effect could not be confirmed for the bainitic and martensitic initial microstructures.

The present study aims at analyzing the effect of heating rate and initial microstructure on austenite formation in a 50CrMo4 steel with focus on the following three issues: (i) austenite nucleation and transformation kinetics, (ii) carbide dissolution, and (iii) austenite homogeneity. To this end, the phase transformation to austenite was studied at heating rates of 1, 10 and 100 K/s for a 50CrMo4 steel for an initial ferritic-pearlitic microstructure on the one hand and an initial soft annealed microstructure on the other. In-situ analysis of the austenite formation was performed during heating a sample in a dilatometer using high energy X-Ray diffraction (HEXRD). This method not only allows a detailed analysis of the chronological evolution of the phase fractions of present phases (ferrite, austenite, carbide) but it also provides detailed information about the crystallographic features, such as chemical homogeneity, strain or dislocation density, of the austenite and the dissolution of carbides. Additionally, DICTRA simulations were performed in order to model the phase transformation and to study the underlying phenomena.

3. **Methods**

The steel investigated in this study was a 50CrMo4 steel with 0.49 wt.% C, 0.71 wt.% Mn, 1.05 wt.% Cr, 0.18 wt.% Mo, 0.27 wt.% Si, 0.016 wt.% P and 0.010 wt.% S.

Two initial microstructures, a ferritic-pearlitic and a soft annealed condition, were produced from the originally rolled 22 mm diameter material by applying heat treatments proposed in literature [10]. The ferritic-pearlitic condition (FP) was adjusted by austenitizing the samples at 850°C for 20 min, followed by cooling to 650°C, a subsequent isothermal treatment at this temperature level for 1500 s and final air cooling of the samples to room temperature (Figure 1a). The soft annealed condition (SA) was produced by austenitizing the samples at 850°C for 20 min followed by quenching in water and annealing of the specimens at 710°C for 7 h with subsequent furnace cooling (Figure 1b).

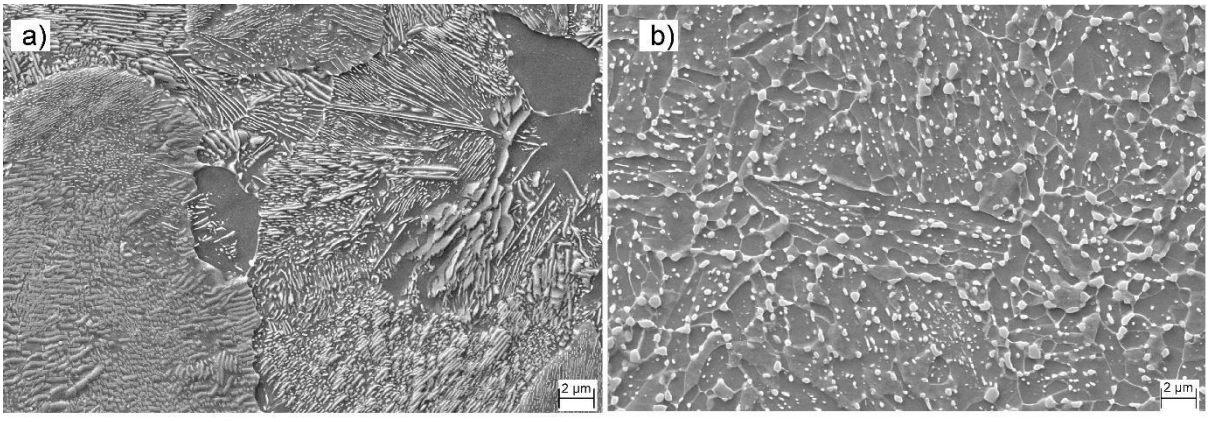

Figure 1: Scanning electron micrographs of the ferritic-pearlitic (a) and soft annealed (b) initial microstructures.

The samples for the in-situ HEXRD experiments exhibited a diameter of 4 mm and a length of 10 mm and were manufactured from half radius position of the 22 mm diameter rod material.

Scanning electron microscopy (SEM) images were acquired using a Zeiss EVO MA25 in secondary electron imaging mode of samples shortly etched with 2% nitric acid. The cementite sizes ($l_{cem,Exp}$) of both initial microstructures were analyzed using the image analysis software Stream Motion. The average cementite diameter of the SA condition is about 190 nm. The average pearlite lamella thickness of the FP state is about 55 nm. Amount of ferrite was 2% forthe FP state, as analyzed by Stream motion.

Samples for nucleation site analysis were heated in the dilatometer with 10 K/s and quenched with 230 K/s after reaching the desired temperatures (790°C). The temperature was chosen to obtain information about the nucleation sites at the beginning of the austenitization. The samples were analyzed using SEM in order to analyze where the austenitic phase nucleates. SEM investigations were conducted at 4 different positions of the samples. For additional EBSD analysis specimens were prepared with a vibratory polisher (Buehler VibroMet 2) using Buehler MasterMet_2 as polishing suspension. The EBSD scans were carried out in the analytical mode with 20 kV and with a step size of 100 nm in a Dual Beam Microscope Versa3D by FEI equipped with an EDAX Hikari XP EBSD system. The data was evaluated using the software tool TSL OIM Analysis 7 software. As data clean up, grain dilation tolerance angle of10.5 deg for the soft annealed and 5 deg. for the ferritic-pearlitic state as well as a minimum size of 5 data points was used.

In-situ HEXRD based analysis was performed during inductive heating of the samples in a dilatometer which was integrated in the high energy materials science (HEMS) beamline (P07)at PETRA III, DESY, Hamburg [12]. The dilatometer used was a Baehr DIL805A dilatometer that was placed into the beam [13] and heating rates of 1, 10 and 100 K/s were applied to heat the specimens from room temperature up to 1050°C. Temperature was measured using a type K thermo couple welded near the position of HEXRD measurement. In order to penetrate the4 mm thick samples, high energy X-rays were used with a photon energy of 87.1 keV, corresponding to a wavelength of 0.14235 Å. The beam size was 0.7 x 0.7 mm and the transmission rate was 27%. The resulting diffraction rings were recorded with a Perkin ElmerXRD1621 flat panel detector which was positioned in a sample detector distance of 1325mm.For the heating rates of 1 and 10 K/s a frame acquisition rate of 5 Hz and an exposure time of0.2 s were chosen, while for 100 K/s an exposure time of 0.1 s was selected. Average temperature during exposure time was correlated to the diffraction patterns. The intensity of the recorded Debye Scherer rings was integrated and exported as a function of 2theta using thefit2D software from ESRF [14]. To evaluate phase fractions and crystallographic characteristics, selected peaks of the phases were fitted using the Pseudo Voigt fit function. The peaks chosen had little or no adjacent peaks of other phases to minimize the effect of overlapping peaks. For ferrite/bcc (space group: I m -3 m) this was the {200} peak, for

austenite/fcc (space group: F m -3 m) as well the {200} peak and for cementite/Fe_3C (space group: P n m a) the {301} peak. Phase fractions were not evaluated quantitatively, but the ratios of the peak areas to the total areas of the peaks depicted according to ASTM-E973-13 [15] were taken as a semi-quantitative information.

Kinetic simulations were conducted with DICTRA4.0 using the TCFE8 and MOBFE3 databases. The moving boundary model was employed. At starting temperature (700°C) the bcc and the cementite (cem) phases were set active, while fcc was set inactive in between bcc and cem. The required driving force, i.e. the nucleation barrier for fcc precipitation was set to the default value of 1e-5 J/mole for a negligible small barrier. Figure 2 depicts a scheme of the simulation setup at the temperature at which the simulation starts (700°C, Figure 2a) and at temperatures higher than A_{c1} (Figure 2b). Except P and S, all elements were considered in the simulation with their weight percentages present in the bulk. The initial cementite thicknesse sin DICTRA ($l_{cem,Sim}$) were set to 10, 20 and 50 nm to roughly cover the range of experimentally determined values, see Table 1. Because of symmetry reasons in the DICTRA model, the cementite thickness $l_{cem,Sim}$ in the DICTRA simulation set-up equals half of the real cementite thicknesses $l_{cem,Exp.}$ As initial composition of the cementite its equilibrium composition at 700°Cwas chosen, calculated with Thermo-Calc. The size of the simulation cell including the bcc thickness as well as the composition of bcc were calculated according to the procedure used by Liu et al. [16], see Table 1, so that the resulting overall chemical composition of the system is in accordance with the chemical composition of the 50CrMo4 steel. The simulation started assuming equilibrium at 700°C and subsequent heating to 1050°C was predicted with heating rates of 1, 10 and 100 K/s. The initial chemical composition and the chosen geometrical set-up are shown in Table 1.

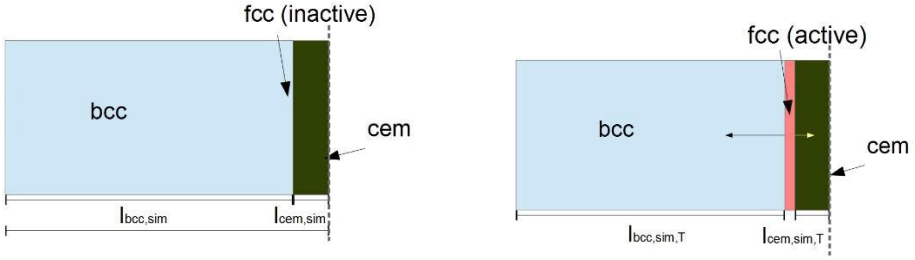

Figure 2: Sketch of the DICTRA set-up. a) depicts the simulation set-up at the start of the simulation (700°C), and b) depicts the set-up of the simulations at temperatures higher than A_{c1}.

Table 1: Initial chemical composition of the bcc and cem phases chosen for the DICTRA simulation as well as the total cell sizes and bcc cell sizes for the three initial cementite half-thicknesses $l_{cem,Sim}$. The inaccuracy of the phase fraction determination was approx. 5- 10% of the respective phase fraction as

determined by HEXRD data.

Chemical compositions of the phases in equilibrium at 700°C					
	C	**Cr**	**Mo**	**Mn**	**Si**
cem	*6.73*	*11.51*	*0.74*	*4.83*	*4.72e-11*
bcc	*5.02e-3*	*0.24*	*0.13*	*0.39*	*0.29*

Phase thickness and cell sizes as calculated by Thermocalc at 700°C			
Set-up	Initial cem half thickness $l_{cem,Sim}$ [nm]	Initial bcc half thickness	Total simulation cell size [nm]
1	10	138	148
2	20	277	297
3	50	692	742

4. Experimental results

a) In-situ investigation of the effect of initial microstructure and heating rate on phase transformation kinetics

For detailed examination of the transformation kinetics, the phase evolution of austenite and cementite was determined by means of the HEXRD experiments during heating. Figure 3ashows the phase transformation kinetics for the FP initial state, while Figure 3b depicts the transformation kinetics for the SA initial state. All transformation start and finish temperatures (A_{c1} = austenite start temperature, A_{c3} = ferrite finish temperature and A_{cc}= cementite finish temperature) were determined from detailed data analysis and are summarized in Table 2.

Figure 3c depicts selected diffraction patterns with increasing temperature for the FP state at 700, 800, and 900°C, respectively, where the peaks of interest for each phase are marked.

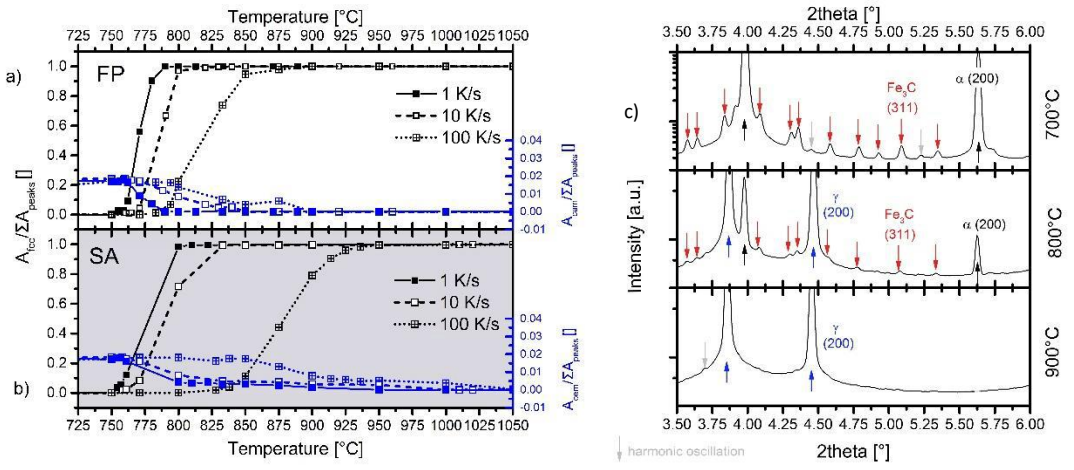

Figure 3: Phase evolution for the FP state of the fcc (black) and cem phases (blue) over temperature for the

FP state (a) and the SA state (b, grey background). The transformation kinetics for the three heating rates are depicted for both states: 1 K/s (solid lines), 10 K/s(dashed lines) and 100 K/s (dotted lines). For the phase fraction evaluation, the peak areas of austenite {200} and cementite {301} are depicted as ratio of the sum of the peak areas of ferrite {200}, austenite {200} and cementite {301}. The inaccuracy of the phase fraction determination was approx. 5- 10% of the respective phase fraction. c depicts diffraction patterns at 700, 800,and 900°C for the FP state heated with 10K/s. Each phase and the peaks of interest are marked.

In Figures 3a and b, all phase evolution curves indicate a sigmoidal trend. In general, the influence of the heating rates is similar for both initial microstructures: with increasing heating rate the transformation temperatures (A_{c1}, A_{c3} and A_{cc}) increase while the slopes of the phase fraction vs. temperature curve decrease. However, the increase of A_{c1} is less pronounced than the increase of A_{c3} and A_{cc}. Cementite starts to dissolve at temperatures higher than A_{c1} and the reduction of the cementite phase fraction follows a sigmodal trend as well until A_{c3} is reached. For the FP sample heated with 1 K/s, cementite dissolution is complete slightly below A_{c3} (see Table 2) while for the SA samples A_{cc} is higher than A_{c3}. At temperatures above A_{c3}, further cementite dissolution within the austenite occurs almost linearly with increasing temperature. Complete dissolution of cementite (A_{cc}) is shifted to higher temperatures with increasing heating rates.

Figures 3a and b indicate that the SA state exhibits higher A_{c3} and A_{cc} temperatures compared to the FP state. The most distinct difference can be observed for the SA sample heated with 100K/s, which exhibits significantly higher transformation temperatures than all other states, and cementite dissolution is even not finished when 1050°C is reached. Figure

b) Analysis of the fcc nucleation sites

The HEXRD data does only provide information about the overall phase fractions but does not allow conclusions concerning the nucleation sites. Hence, nucleation site analysis was conducted using interrupted heating experiments. Figure 4a and b depicts a micrograph of the FP state quenched after reaching a temperature of 790°C. Phase identification in the SEM image was done optical through the degree of etching, since the martensitic areas formed from fresh austenite are less etched than pure ferritic areas and differences in contrast within SEM images are observed. The areas marked with green framing were identified as purely ferritic areas, while the areas marked with red framing are martensitic areas, which were originated from freshly formed austenite. It is visible that at 790°C the austenitic areas are often formed at the interfaces between ferrite and perlite or pearlite and pearlite and within pearlite grains. This trend was observed across the whole sample. Using EBSD analysis the grain average misorientation (GAM) is depicted, since a high misorientation can be associated to martensitic areas. In the FP state the light green and white areas can be contributed to martensite. These areas are in accordance to the areas marked in the SEM image.

In Figure 4b the results of a similar investigation are shown for the SA state. It seems that an appreciable number of martensitic areas is present next to spherodized cementite. Optical evaluation indicates that the SA state exhibits a higher number of martensitic areas, while the martensitic features in the FP state are larger in area. This trend is reproduced within the GAM image of the SA state in Figure 4d. A higher number and smaller size of the white areas within the GAM is visible. Additionally, it needs to be mentioned, that the grain size of the SA-state is significantly smaller than the grain size of the FP state.

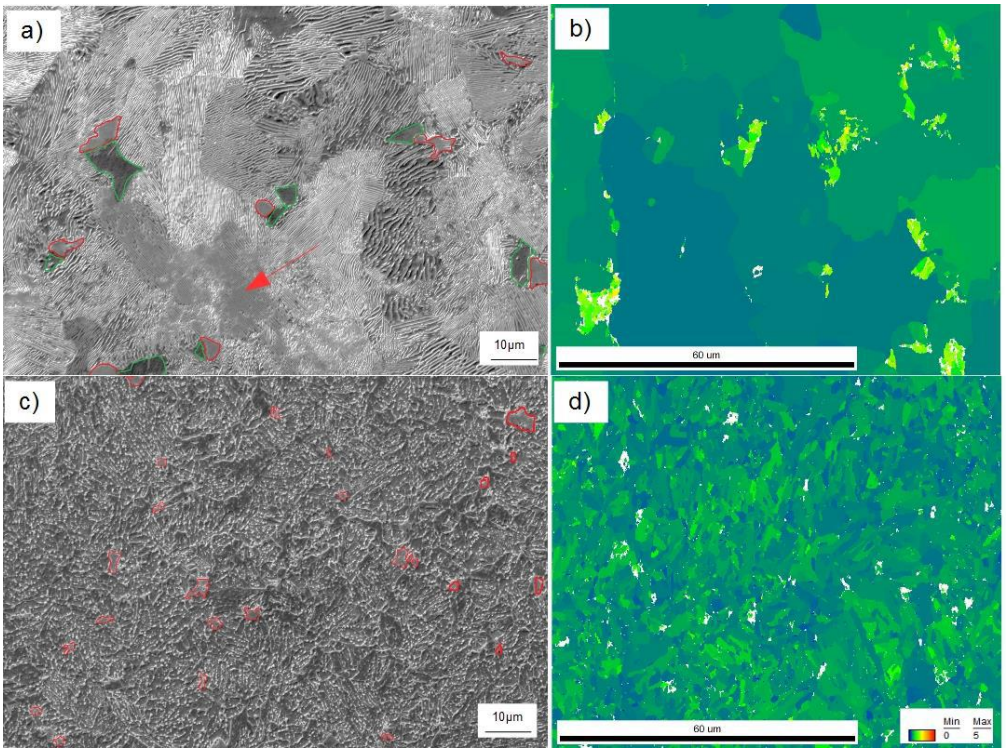

Figure 4: SEM and EBSD GAM images of interrupted heating with 10 K/s to 790°C of the FP-state (a, b) and the SA state (c,d). The red-encircled areas in a) and c) refer to martensite areas, while the green-encircled areas in a) refer to ferrite areas. The white and light green areas in the GAM images correspond to areas with high disorientation, i.e. martensite.

c) Evolution of the lattice constant and the full width at half maximum of the austenitic state

Carbon content and homogeneity of the austenite formed during heating were analyzed by evaluation of the lattice constant and the full width at half maximum (FWHM) of the reflections.

In Figures 5a and d the overall trends of the lattice constants of the FP and SA conditions are shown. For all heating rates and initial microstructures, the lattice constant starts at a higher level and decreases until it reaches a minimum between A_{c1} and A_{c3}. At higher temperatures, it increases linearly with temperature, which is mainly ascribed to the thermal expansion of the austenite.

Comparing the different initial microstructures the minimum lattice constant values (Figures 5aand d) are lower for the SA state compared to the FP state. For the heating rate of 1 K/s this difference is negligible, while for 10 and 100 K/s the difference is significant. Additionally, the minimum of the lattice constant is shifted in case of the FP state to higher temperatures, in accordance with the behavior of A_{c3}

temperature.

To visualize the differences in the lattice constant over temperature in austenite, a reference needed to be set. To obtain a reference curve of the linear expansion of the lattice constant of this particular steel, the trend of the lattice constant of FP state heated with 1 K/s (FP-1K/s) was chosen. At temperatures higher than A_{c3} the material is fully austenitic and all cementite, hence all alloying elements, are dissolved within the matrix. A linear fit of the experimental data of FP-1K/s was done between A_{c3} and 1050°C to obtain the linear expansion of the lattice constant over temperature (red line in Figure 5a, slope m). The experimentally determined lattice constant values were subtracted from that of the reference line for the respective temperature (Figures 5 b and e). The difference to the reference line is increasing with increasing heating rate for both states, whereas the difference is higher for the SA state and remains present up to higher temperatures compared to the FP state. The thermal expansion coefficient calculated for this reference curve is $24.8e^{-6}\,K^{-1}$ [17]. Comparison of chemical composition at room temperature was done according to Cheng et al [18] and determined to be 2.53at.%. The initial carbon concentration is 2.23 at% C, hence carbon content with is in good range with the steel composition.

The values of FWHM for the SA and FP conditions (depicted in Figures 5c and f) start at high levels for all initial states and are subsequently decreasing with increasing temperatures. This decrease is shifted to higher temperatures at higher heating rates.

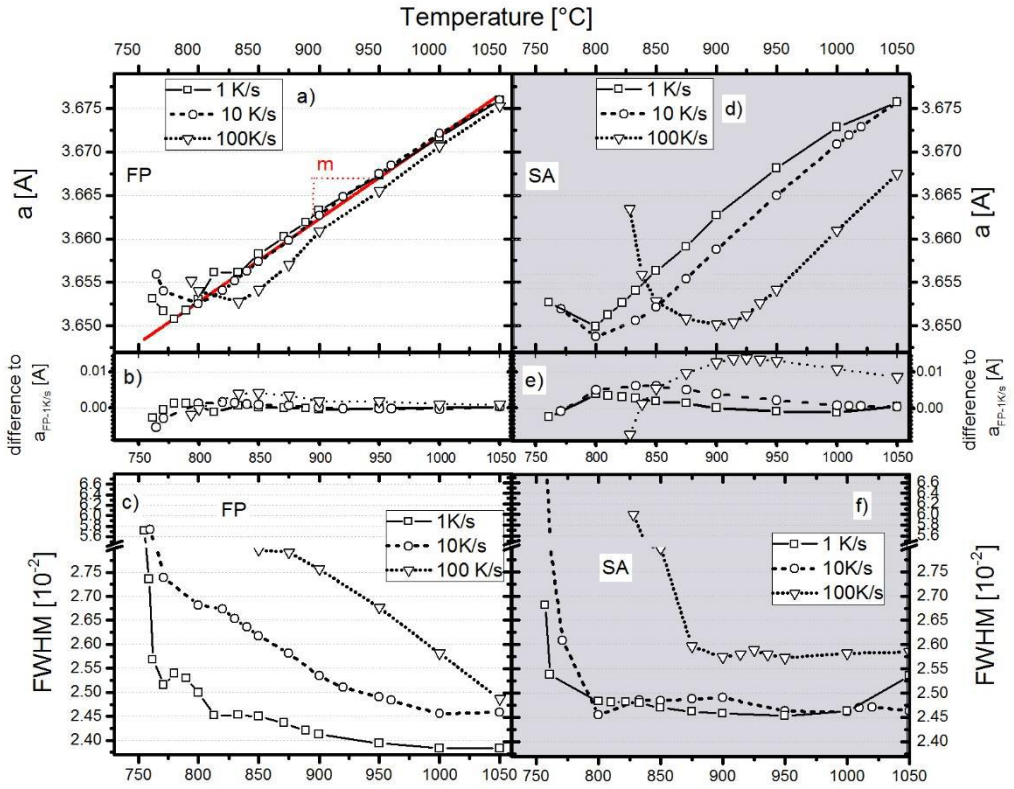

Figure 5: Lattice constant and FWHM of the fcc peak depicted over temperature for the FP initial state (a,c,) and SA initial state (d,f). The difference of the experimentally determined lattice constant and the linearized reference line for FP-1K/s (red line in a) is shown for both initial states in b) (FP) and e) (SA). All three heating rates are depicted in every diagram (1 K/s solid line, open square, 10 K/s dashed line,

open circle and 100 K/s dotted line, open triangle).

However, while the FP state shows a constant decrease of FWHM with increasing temperature, the SA state exhibits a more drastic decrease shortly after the maximum and then remains at a constant level with increasing temperature. Reaching of the constant value of FWHM coincides for the SA state with the temperature of the lattice constant minimum for all three heating rates. In case of SA states, the heating rate of 100 K/s exhibits a significantly higher value of the plateau value of the FWHM compared to that achieved with heating rates of 1 and 10 K/s.

5. Computational corroboration

a) Simulation of the transformation kinetics using DICTRA

Second focus of this study is to simulate the phase transformation and the homogeneity of the austenitic state numerically using the software tool DICTRA. To this end, different initial cementite thicknesses as well as heating rates were investigated and the results were compared to the results obtained from HEXRD.

Figures 6a and b depict the phase transformation as a function of heating rate (a) and cementite half thickness $l_{cem,Sim}$ (b). A first general conclusion is that the sigmoidal phase transformation trend observed in the experiments is largely reproduced by the DICTRA simulation. Additionally, with increasing heating rate (Figure 6a) the onset of the phase transformation shows a more sluggish behavior, which is also accompanied by higher A_{c3} temperatures. For a constant heating rate of 10 K/s, an increasing $l_{cem,Sim}$ shifts the fcc phase fraction curve towards higher temperatures. Thus, the cementite dissolution occurs more slowly with increasing $l_{cem,Sim}$.

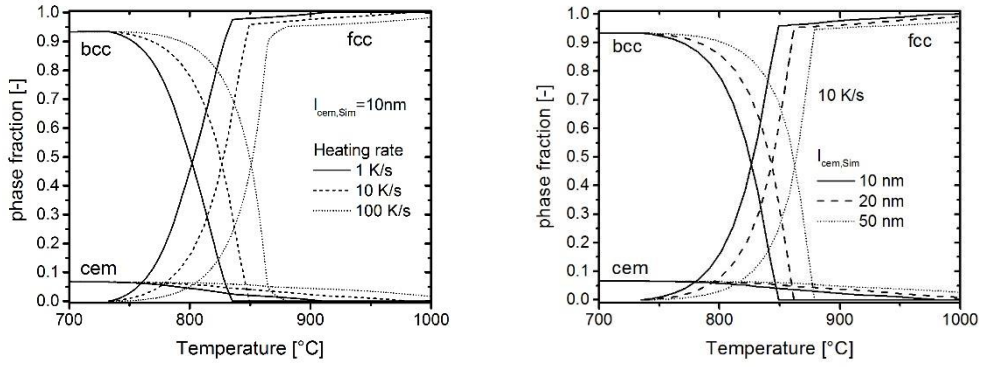

Figure 6: Simulation of the evolution of phase fractions of bcc, fcc and cem for different heating rates (a) and 3 different cementite half thicknesses (b). Solid lines refer to an initial $l_{cem,Sim}$ of10 nm, dashed lines to 20 nm and dotted lines to 50 nm.

The DICTRA simulations reproduce the trends observed from the experiments as indicated by the results summarized in Table 2. With higher heating rates and larger $l_{cem,Sim}$, the transformation temperatures are increasing. For all heating $l_{cem,Sim}$ of 10 nm matches the values of the FP state, while $l_{cem,Sim}$ of 50 nm

fits the values of the SA state. Considering the temperature at which all cementite is dissolved (A_{cc}), the simulation results yield somewhat higher temperatures than found in the experiments. For high heating rates and the largest $l_{cem,Sim}$(100 K/s: for all $l_{cem,Sim}$; 1 K/s and 10 K/s: $l_{cem,Sim}$= 50nm) the A_{cc} temperature was not achieved at the end of the simulation at 1050°C. Such a behavior was also experimentally observed for the SA initial state heated with 100 K/s, where a cementite peak was still present at 1050°C.

Table 2: Summary of all transformation temperatures with respect to the heating rates.

Experimental (Exp) data is marked with a grey background, the other data was derived from DICTRA calculations. The simulations and experiments were performed to a temperature up to1050°C; T > 1050°C in the table indicates that A_{cc} was not reached up to this temperature level. Uncertainty of temperature values are mainly due exposure time of data collection and measuring inaccuracies: Heating rate 1 K/s: Temperature uncertainty ~ 1 K; Heating rate10 K/s: Temperature uncertainty ~ 2 to 3 K; Heating rate 100 K/s: Temperature uncertainty ~5 to 10 K

Heating rate [K/s]	State /	$l_{cem,Sim}$	A_{c1} [°C]	A_{c3} [°C]	A_{cc} [°C]
1	Exp	FP	755	800	785
		SA	752	815	925
	DICTRA	10nm	733	835	910
		20nm	734	854	955
		50nm	738	862	> 1050
10	Exp	FP	763	830	845
		SA	760	880	970
	DICTRA	10nm	735	842	981
		20nm	737	862	1026
		50nm	741	879	> 1050
100	Exp	FP	775	860	890
		SA	810	940	> 1050
	DICTRA	10nm	739	881	> 1050
		20nm	743	874	> 1050
		50nm	747	898	> 1050

b) Computational investigation of the homogeneity of the freshly formed austenite

For examination of the homogeneity of the austenite, the chemical composition across the simulation

cell was calculated, results are depicted in Figure 7 for the point when a temperature of 950°C (a) 1000°C (b) and 1050°C (c) is reached in case of heating with 10 K/s and an initial cementite thickness of 20 nm ($l_{cem,Sim}$= 10 nm). The dissolution of cementite takes still place at950°C and thus the concentration of Cr, Mn and C in fcc near the cementite interface is highand decreases with increasing distance from the interface. Chromium exhibits the highest gradient within austenite, followed by manganese. Chromium concentration in fcc increases up to 6 at.% near the interface and increases up to 36 at.% within cementite. The same trend is stillpresent at 1000°C. Although the cementite has dissolved completely when reaching 1000°C ata heating rate of 10 K/s, especially chromium has not homogenized over the simulation cell yet.The chromium concentration varies in a range of about 0.3 to 3.6 wt.% over the length of thecell. Local differences in carbon concentration are much smaller but still present, the carbon content varies between about 0.4 to 0.6 wt.%. Looking at a higher temperature of 1050°C (Figure 7c) it is obvious, that homogenization has almost fully taken place. Comparing theresults of 10K/s to the results of 100K/s and $l_{cem,Sim}$ =10nm (Figure 7d and e) it needs to bestated, that 100K/s leads to less homogeneity at equal temperatures compared to a heating rateof 10K/s.

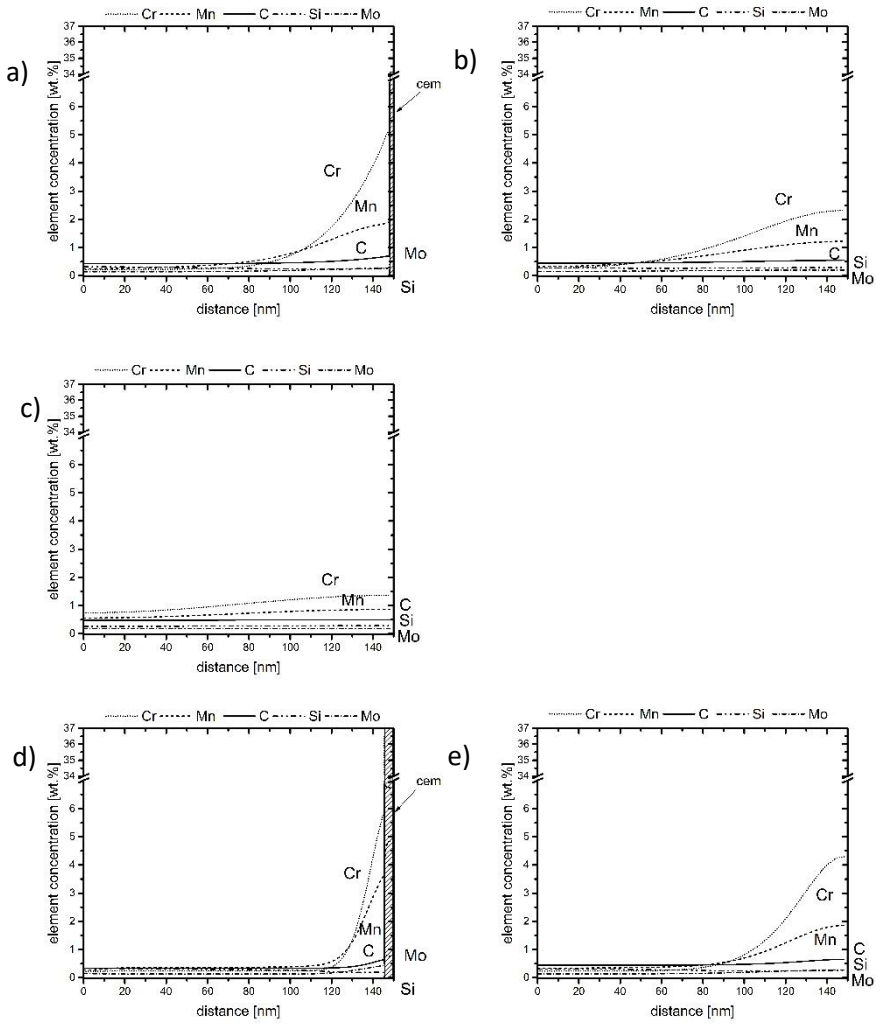

Figure 7: Element concentration distribution in fcc calculated with DICTRA by using the setup shown in Figure 1 and a heating rate of 10 K/s and an initial cementite half thickness $l_{cem,Sim}$ *of10 nm at 950°C (a), 1000°C (b) and 1050°C (c). Additionally, chemical profiles of 100K/s and* $l_{cem,Sim}$ *= 10nm is depicted for 950°C (d) and 1050°C (e).*

6. Discussion

The following discussion concentrates (a) on the factors that influence the transformation temperatures, (b) on the analysis of the stages of austenite formation and the austenite homogenization , and (c) on the evaluation of the DICTRA results.

a) Dependence of transformation temperatures from ferrite to austenite on heating rate and initial microstructure

Independent of heating rates and initial microstructure, the phase transformation curves exhibit sigmoidal trends (Figure 3) which is in accordance with earlier findings [4]. The transformation temperatures A_{c1} and A_{c3} increase with increasing heating rate as listed in Table 2. The temperature shift of A_{c3} to higher temperatures is higher than that of A_{c1} when increasing the heating rate. This is in line with common time temperature austenitizing diagrams, as already published by e.g. the Max Planck Institut für Eisenforschung [10], according to which the transformation temperatures are shifted to higher temperature values with increasing heating rates. The phase transformation from ferrite to austenite is diffusion controlled and thus an increasing heating rate reduces the diffusion length of the present alloying elements. As a consequence, higher temperatures are needed for sufficient alloying element diffusion and, therefore, the transformation temperatures increase.

Figure 3 also shows the influence of the initial microstructure on the transformation behavior. For all heating rates, the SA state exhibits higher transformation temperatures (A_{c1} and A_{c3}) compared to the FP state. However, A_{c1} is not as strongly changed over all states as A_{c3}. A_{c1} seems almost uninfluenced by the heating rate, since the nucleation of austenite occurs at ferrite-cementite interfaces for both states. Hence, outward diffusion of carbon and other alloying elements at the interface of the cementite is the controlling step for austenite nucleation, which is almost independent of cementite size or morphology. The drastic shift in A_{c1} temperature for SA-100K/s to higher values is supposed to be due to insufficient time for the release of carbon with its strong chemical bonds within the cementite particles.

On the contrary, A_{c3} increases drastically comparing the different initial microstructures. The ongoing outwards diffusion of carbon from the cementite is necessary to increase austenite volume fraction. However, outward diffusion of carbon is impeded for larger spherical cementite particles, as present within the SA state, due to higher diffusion length out of the particles and less surface area of the particles. On the other side, pearlite lamellas (FP-state) exhibit less cementite thickness and higher surface area compared to the spherical cementite (SA-state) particles, which is beneficial for outward carbon diffusion.

Stages of austenite formation

The classification of the different formation steps, as depicted in Figure 8, is based on significant points within the phase evolution as well as on the development of the lattice constant for all evaluated states.

The first stage is marked by the first occurrence of austenite (I). The second stage represents the decrease of the lattice constant to a minimum (II) and the third stage is connected with an increase of the lattice constant and confined by A_{c3} (III).

Austenite formation mainly takes place in the stages II and III and is to a large extent a result of the transformation of ferrite to austenite and to a smaller extent a result of cementite dissolution. The fourth stage (IV) is connected with the ongoing dissolution of cementite and is thus confined by A_{cc}, and in the final stage (V) homogenization of the austenite takes place during further heating.

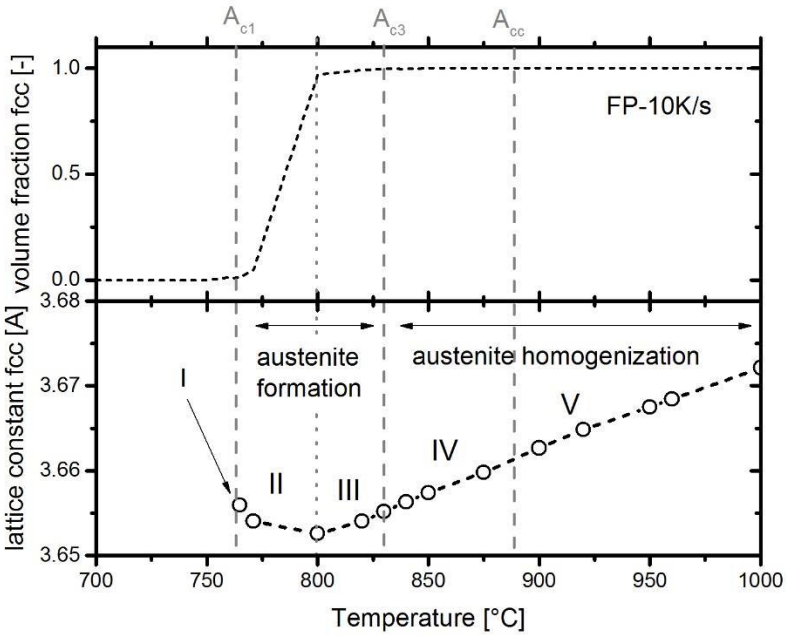

Figure 8: Austenite volume fraction and lattice constant evolution when heating a 50CrMo4-steel in a FP state with a constant heating rate (results were taken from Figures 3 and 5).

Stage I: Nucleation and early growth of carbon rich austenite

Nucleation of the austenitic phase within the ferrite-cementite matrix are depicted in Figure 4.For the FP state, nucleation sites are located mostly at the interfaces between ferrite and pearlite grains. However, also areas are observed, where austenite has nucleated within pearlite grains, probably at the interfaces of ferrite and the cementite lamellas. Both observations are in line with literature [20, 11]]. The nucleation sites within the SA microstructure appear to be at the interfaces between the large spherodized cementite particles and the ferritic matrix. In both microstructures the cementite is providing the carbon for the fcc nucleation and further growth. In the FP state the cementite is present within large pearlite grains, hence cementite can be provided within a large prior pearlite grain: nucleation is within pearlite grains at the interfaces between cementite and ferrite. Within the SA state austenite is nucleating at the cementite particles, and needs to grow from the carbide into the ferritic matrix. More nucleation sites compared to the FP states are present.

In Figure 5, the austenite lattice constant starts at a high value for all states (Figures 5a and d).It is widely accepted, that the austenite lattice constant increases with the amount of elements dissolved in the matrix (in this case C, Cr, Mn, Mo) or with temperature due to more vibrant lattice oscillations [20, 21, 22]. Since austenite nucleates at the interfaces of ferrite and cementite it is enriched with carbon. The higher the carbon concentration (up until eutectoid composition) the lower the equilibrium A_{c1} temperature will be. Hence, it is suggested that the freshly formed austenite obtains a chemical composition close to eutectoid carbon concentration.

Regarding the FWHM results of both states, the FWHM has its highest values at the beginning of the transformation (see Figure 5). The possible effects causing an increase of the FWHM of a phase are decreasing crystallite size, increasing dislocation density and elastic strains within crystals, while the peak width decreases with increasing homogeneity of the chemical composition [23]. At the beginning of the austenite formation, the high FWHM might be due to the small crystallite size of the freshly formed austenite. Directly after beginning of the austenite formation the FWHM is higher for the SA than for the FP state, which leads to the conclusion that the freshly formed austenite areas are smaller in the SA state than in the FP-state. This is affirmed by the evaluation of Figure 4, which showed a higher number of nucleation sites and smaller austenite areas for the SA than the FP state. However, also the chemical homogeneity of the freshly formed austenite might influence the FWHM during the early stages. As cementite dissolves, an enrichment of carbon within the austenite regions next to the cementite will be present, and thus, a chemical gradient establishes within the freshly formed austenite. Since the austenite formation is diffusion controlled, it is assumed that an increase of dislocation density within the freshly formed austenite, which influence FWHM, can be neglected.

Stage II: Growth of austenite phase fraction and reduction of carbon content in austenite

During the second stage of austenite formation, the phase fraction of austenite shows a major increase. Simultaneously, the lattice constant is decreasing to a minimum (Figures 5a and d)and all states show the same trend. During the decrease of lattice constant the freshly formed austenite, which exhibits a high carbon content close to eutectoid composition upon nucleation(stage I), is growing in volume fraction and the content of alloying elements (especially Cr, C)within the austenite is decreasing. Depletion of alloying elements is necessary to obtain the overall composition of the 50CrMo4 steel compared to the highly enriched austenite upon nucleation. This depletion of alloying elements is responsible for the decrease of the lattice constant in stage II.

Stage III: Completion of austenite formation and thermally conditioned lattice constant increase

The minimum of the lattice constant marks the transition from the second to the third stage. In the third stage the remaining small ferrite phase fractions are transformed into austenite (see Figure 4). Simultaneously, the lattice constant is going to increase, which results in an almost linear increase of the lattice constant with increasing temperature. That is in line with literature since the lattice constant is linearly temperature dependent for a steel with a certain chemical composition [22, 24]. A possible

explanation for the constant linear increase might be that as soon as the austenite nearly gains the overall chemical composition of the 50CrMo4 steel, the lattice constant is mainly increasing due to the rising temperature. Consequently, the finally formed austenite would have the overall chemical composition of the 50CrMo4 steel. However, since the lattice constant for all states is still somewhat lower than the reference lattice constantFP-1K/s (Figures 5b and e), where all cementite is dissolved at A_{c3}, it can be assumed, that at the beginning of stage (III) the austenite composition is close to the overall composition of the steel. But, since not all cementite has been dissolved, the lattice constant is still subject to slight changes caused by ongoing carbon dissolution.

Stage IV: Completion of cementite dissolution and ongoing homogenization and strain relieve

The cementite dissolution behavior is depicted in Figures 3a and b. During the ferrite to austenite transformation, cementite dissolution is showing a sigmoidal trend. As soon as A_{c3} is reached, cementite seems to dissolve almost linearly with increasing temperature in all states 457 (except FP 1K/s). The sigmoidal trend at the beginning of the ferrite-austenite transformation is due to the typical trend in nucleation theory according to Johnson-Mehl-Avrami- Kolmogorov (JMAK) equation [26]. At temperatures below A_{cc}, the diffusion of alloying elements from the dissolving cementite into the austenite becomes the determining step for the dissolution of cementite.

During cementite dissolution, the lattice constant of the austenite increases with the increasing content of dissolved elements within the austenite matrix. At higher heating rate the lattice constant always exhibits a lower value at equal temperatures for both the FP and the SA state, with the latter generally having the smaller lattice constant. This effect is more distinct at the 466 higher heating rates 10 and 100 K/s and is due to the lower amount of alloying elements dissolved within the matrix.

As shown in Table 2, the A_{cc} temperatures increase with increasing heating rates. This is again due to the diffusional character of the cementite dissolution. Higher heating rates require higher temperatures to enable diffusion of the alloying elements out of the cementite. Due to the larger cementite size of the SA state its A_{cc} temperature is higher than the corresponding A_{cc} temperature of the FP state at all three heating rates. Since cementite is dissolving via its surface it takes more time to dissolve a large spherical cementite particle with less specific surface area compared to the thinner cementite lamellas in pearlite with a higher specific cementite surface area.

The results indicate that the cementite dissolution temperature (A_{cc}) is highly dependent on the initial cementite size. Due to the larger cementite particle size of the SA state (190 nm average diameter) compared to pearlite lamella thickness of the FP-state (55 nm) the dissolution of cementite in the SA state needs higher temperatures (this is reflected by its higher A_{cc} temperatures).

The development of the FWHM in Figure 5a and 5b as function of the temperature leads to the conclusion that an inhomogeneous carbon distribution might play a major role, but some effects caused by strain

relieve cannot be excluded.

It can be concluded from the results that Stage IV is only present in case of higher heating rates and larger initial cementite thicknesses.

Stage V: Ongoing homogenization and strain relieve in austenite

To evaluate the austenite homogeneity the results of the FWHM (Figures 5c and f) need to be discussed in regard to all effects contributing to the FWHM.

The homogeneity of the austenitic phase with respect to the alloying element supposed to be the main influencing factor on the FWHM in Stage V, but the straining of austenite crystals as a result of its fast growth is supposed to have an influence too. For the FP state, the FWHM shows a constant decrease over the investigated temperature range. This phenomenon is assumed to be mainly due to the inhomogeneous alloying element distribution (immediately) after transformation. The austenite formed from the initial pearlitic grains achieves a very high alloying element concentration, while the austenite formed from the initial ferrite grains has not achieved a homogeneous alloying element distribution when cementite is completely dissolved and the material enters stage V during heating. With further increasing temperature and time and thus enhanced diffusion the alloying element distribution becomes more homogeneous and strains at crystal level caused by the inhomogeneities are reduced due to recovery and grain growth.

Effects of the grain size on the FWHM are only supposed to play a role at the nucleation stage of austenite. It is assumed that the influence of the austenite grain size on the FWHM ends at least at A_{c3}, the further increase in grain size is not supposed to affect the FWHM during further heating. After an austenite grain size of 1 µm is reached, the contribution of austenite grain size is as low as 1.35e-4 2theta (calculated by [23, 26, 27]), while experimental values decrease by at least 1*e-3 for the FP state after reaching A_{c3}, or remains constant for the SA state. Hence austenite grain size is assumed to have only a negligible effect on the FWHM after A_{c3} is reached [28]. The existence of sub grains as well as relieving strain of the freshly formed austenite grains cannot be completely excluded as a reason for the decrease of FWHM.

However, the trend in FWHM correlates nicely with the suspected trend of homogenization within the austenite matrix.

At the heating rate of 100 K/s, the FWHM of the SA state does not decrease to the same value as the other states. For this sample A_{cc} lies beyond1050°C, and thus cementite is still dissolving and releases its alloying elements into the matrix. The constant higher level seems to be a steady state depending on dissolving cementite, ejection of alloying elements into the austenite matrix and diffusion controlled

homogenization of these elements in the austenite. A further reason for the higher level of the FWHM of the SA state might be the very short time since the material is just about 3 s at a temperature above 750°C until reaching 1050°C. There is thus also a very short time available to relieve strains and crystal defects. The results demonstrate, that especially for high heating rates higher temperatures are beneficial for achieving a homogeneous austenite with all cementite fully dissolved. After completion of the cementite dissolution even higher temperatures are needed to enable especially chromium diffusion within the austenite and to homogenize the chemical composition.

It is assumed that Stage V is present in all initial states for technically relevant heating rates.

Comparing the HEXRD data with previously mentioned literature [4], data evaluation was done in far more detail and FWHM and lattice constant development was conducted on the in situ 529 data, which had not been done before in this way.

Evaluation of DICTRA simulation

DICTRA is a powerful tool to simulate diffusion controlled transformations [29, 4]. Summarizing the comparison of DICTRA simulation and experimental results it can be concluded, that the simulation describes the experimental observations accurately.

Regarding the phase transformation, the DICTRA results show a sigmoidal phase evolution as well as an increase in transformation temperature with increasing heating rate and cementite half thickness $l_{cem,Sim}$. A certain deviation from the experimentally determined transformation temperatures needs to be accepted (Table 2). Neither nucleation mechanisms nor 3D diffusion is considered within the DICTRA simulation. Additionally, the interface energy of cementite is not considered. Hence differences in transformation temperatures occur, comparing simulation and experimental temperatures. This might be due to the moving boundary setup that is more accurately fitting the features of the lamellar cementite present in the FP state. Cementite half thickness within the simulation needs to be adapted to smaller thicknesses to account for the spherodized cementite particles present in the SA state. In order to use DICTRA to predict transformation temperatures, cementite thickness needs to be adjusted carefully, since the simulation is underestimating the actual cementite size.

Interesting insights are provided by the chemical profile across the simulation cell (Figure 7)during cementite dissolution and austenite homogenization. Especially the increased chromium concentration at the interface of cementite and austenite is an indication, that chromium but not the carbon diffusion diffusion out of the cementite is the time controlling step during dissolution. In the dissolved state, only a slight gradient in carbon may occur on µm-scale range, while a larger chromium gradient can be assumed, which needs higher temperatures to homogenize ($D_{C,1000°C}$=3.02*e-11 m^2s^{-1}; $D_{Cr,1000°C}$=3,04*e-16 m^2s^{-1}). Applying the diffusion length of carbon and chromium at elevated temperatures and the experimental A_{cc} temperatures as well as the largest distances between cementite particles, it becomes obvious, that carbon homogeneity should not be a problem. However, the chromium diffusion path is at

maximum 557 0.6 µm at 1050°C (applying a heating rate of 1 K/s), hence, inhomogeneities can be expected 558 with regard to chromium especially at the at lower temperatures.

7. **Conclusion and Summary**

This study shows the effect of two different initial microstructures and three applied heating 562 rates on the austenite formation, cementite dissolution and austenite homogeneity during fast 563 heating of a 50CrMo4 steel. The presented results lead to the following conclusions:

- Based on the evolution of the lattice constant and phase fractions of fcc, bcc and cementite, five stages of austenite formation are suggested independent on initial microstructure and heating rate:

Stage I. Nucleation and early growth of carbon rich austenite,
Stage II. Growth of austenite phase fraction and reduction of carbon content in austenite
Stage III. Completion of austenite formation and thermally conditioned lattice constant increase
Stage IV. Completion of cementite dissolution and ongoing homogenization and strain relieve
Stage V. Ongoing homogenization and strain relieve in austenite

- Comparing the two initial microstructures, a ferrite-pearlite microstructure exhibits a comparable austenite homogeneity at lower temperatures compared to the solution annealed microstructure. This is due to the slower cementite dissolution of the spherodized cementite,as well as the fact, that only ferritic areas are transforming into austenite. Thus, chemical inhomogeneities in the austenite formed from pearlite and ferrite grains needs to be balanced, which requires higher temperatures and/or longer times.

- For both initial microstructures, higher heating rates (10 and 100 K/s) require higher temperatures to obtain comparable austenitic states in terms of homogeneity and dissolution of cementite compared to 1K/s. The increase in temperature for comparable homogeneity from 1 K/s to 10 or 100K/s is lower for the soft annealed state compared to the ferritic-pearlitic state.

- In general transformation temperatures increase with increasing heating rate and increasing cementite half thickness.

- DICTRA simulation require a careful interpretation since the simulation set-up is more suited for cementite lamellas than for spherodized cementite particles. Within the simulation, chromium diffusion out of the cementite is the rate determining step for cementite dissolution.

Acknowledgement

The authors gratefully acknowledge the financial support under the scope of the COMET program within the K2 Center “Integrated Computational Material, Process and Product Engineering (IC-MPPE)” (ProjectNo859480). This program is supported by the Austrian Federal Ministries for Transport, Innovation and Technology (BMVIT) and for Digital and Economic Affairs (BMDW), represented by the Austrian research funding association (FFG),and the federal states of Styria, Upper Austria and Tyrol.

Data availability statement

The raw/processed data required to reproduce these findings cannot be shared at this time due to echnical or time limitations.

Bibliography

[1] Sackl, S., Leitner, H., Zuber, M., Clemens, H., and Primig, S. *Metallurgical and Materials Transactions A* **45**(12), pp. 5657–5666 (2014).

[2] Vieweg, A., Ressel, G., Prevedel, P., Marsoner, S., and Ebner, R. *Conference proceedings of the 23rd IFHTSE Congress* , 216–222 (2016).

[3] Caballero, F., Capdevila, C., and de Andres, C. G. *Materials Science and Technology***17**(9), 1114–1118 (2001).

[4] Esin, V., Denand, B., Bihan, Q. L., Dehmas, M., Teixeira, J., Geandier, G., Denis, S.,Sourmail, T., and Aeby-Gautier, E. *Acta Materialia* **80**(0), 118 – 131 (2014).

[5] Li, Z.-D., Miyamoto, G., Yang, Z.-G., and Furuhara, T. *Scripta Materialia* **60**(7), 485 –488 (2009).

[6] Oliveira, F., Andrade, M., and Cota, A. *Materials Characterization* **58**(3), 256–261(2007).

[7] Martin, D. S., del Castillo, P. R.-D., and de Andres, C. G. *Scripta Materialia* **58**(10),926 – 929 (2008).

[8] de Andrés, C. G., Caballero, F., Capdevila, C., and Álvarez, L. *MaterialsCharacterization* **48**(1), 101–111 (February 2002).

[9] Beneteau, A., Weisbecker, P., Geandier, G., Aeby-Gautier, E., and Appolaire, B.

Materials Science and Engineering: A **393**(1â??2), 63 – 70 (2005).

[10] Orlich, J. *Atlas zur Wärmebehandlung der Stähle*. Max-Planck-Institut fürEisenforschung, (1973).

[11] Shtansky, D., Nakai, K., and Ohmori, Y. *Acta Materialia* **47**(9), 2619 – 2632 (1999).

[12] King, A., Beckmann, F., Müller, M., Schreyer, A., Schell, N., and Fischer, T. In *Mechanical Stress Evaluation by Neutrons and Synchrotron Radiation VI*, volume 772 of *Materials Science Forum*, 57–61. Trans Tech Publications, 2 (2014).

[13] Staron, P., Fischer, T., Lippmann, T., Stark, A., Daneshpour, S., Schnubel, D., Uhlmann,E.,

Gerstenberger, R., Camin, B., Reimers, W., Eidenberger, E., Clemens, H., Huber, N., and 635 Schreyer, A. *Advanced Engineering Materials* **13**(8), 658–663 (2011).

[14] Hammersley, A. P. *ESRF Internal Report* **ESRF97HA02T** (1997).

[15] ASTM-E975-13. *Standard Practice for X-Ray Determination of Retained Austenite inSteel with Near Random Crystallographic Orientation*, (2008).

[16] Liu, Z.-K., Höglund, L., Jönsson, B., and ågren, J. *Metallurgical Transactions A* **22**(8),1745–1752 Aug (1991).

[17] Onink, M, Tichelaar F.D., Brakman, C.M., Mittemeijer, E.J., von der Zwaag, S; Z.

Metallkd. 87 (1996)

[18] Cheng L. Böttger A., de Keijser Th.H., Mittemeijer E.J., Scripta Metallurgica 24 pp509-514, Dec. (1989)

[19] G.R., S. and Szirmae. *Transactions of the Metallurgical Society of AIME journal* **245**,1074 (1969).

[20] Feng, Z. Master's thesis, Case western reserve university, (2015).

[21] Irvine, K. *High-strength austenitic stainless steels*. (1961).

[22] Seki, I. and Nagata, K. *ISIJ international* **45**(12), 1789–1794 (2005).

[23] Cullity, B. and Stock, S. *X-Ray Diffraction*, volume Third Edition. Prentice Hall, (2001).[24] Cheng, L., Böttger, A., De Keijser, T. H., and Mittemeijer, E. *Scripta metallurgica etmaterialia* **24**(3), 509–514 (1990).

[25] M.Avrami The Journal of Chemical Physics, Volume 9, Issue 2, 1941, Pages 177-184

[26] Zak, A. K., Majid, W. A., Abrishami, M. E., and Yousefi, R. *Solid State Sciences* **13**(1),251–256 (2011).

[27] Yogamalar, R., Srinivasan, R., Vinu, A., Ariga, K., and Bose, A. C. *Solid State*

Communications **149**(43-44), 1919–1923 (2009).

[28] Eggbauer A, Lukas M, Prevedel P, Panzenböck M, Ressel G, Ebner R, *Steel research***accepted** (2018).

[29] Borgenstam, A., Höglund, L., Ågren, J., and Engström, A. *Journal of Phase Equilibria***21**(3), 269 May (2000).